AGU PUBLICATIONS

Geochemistry, Geophysics, Geosystems

RESEARCH ARTICLE
10.1002/2015GC005978

Receiver function imaging of the mantle transition zone beneath the South China Block

Haibo Huang[1], Nicola Tosi[2,3], Sung-Joon Chang[4], Shaohong Xia[1], and Xuelin Qiu[1]

[1]CAS Key Laboratory of Marginal Sea Geology, South China Sea Institute of Oceanology, Chinese Academy of Sciences, Guangzhou, China, [2]Department of Astronomy and Astrophysics, Technische Universität Berlin, Berlin, Germany, [3]Department of Planetary Physics, German Aerospace Center (DLR), Berlin, Germany, [4]Division of Geology and Geophysics, Kangwon National University, Chuncheon, South Korea

Key Points:
- Mantle discontinuities beneath the South China Block were imaged using receiver functions stacking
- The inferred thickness of the transition zone supports the presence of the Hainan plume
- Uplifting of the 660 km discontinuity may be indicative of lateral flow of the Hainan plume

Supporting Information:
- Supporting Information S1
- Data Set S1

Correspondence to:
H. Huang,
go223@scsio.ac.cn

Citation:
Huang, H., N. Tosi, S.-J. Chang, S. Xia, and X. Qiu (2015), Receiver function imaging of the mantle transition zone beneath the South China Block, *Geochem. Geophys. Geosyst.*, *16*, 3666–3678, doi:10.1002/2015GC005978.

Received 1 JUL 2015
Accepted 1 OCT 2015
Accepted article online 6 OCT 2015
Published online 27 OCT 2015

Abstract Upper mantle discontinuities are influenced by convection-related thermal heterogeneities arising in complex geodynamic settings. Slab rollback of the Pacific plate and mantle upwelling in the Meso-Cenozoic caused the extension and spreading of continental segments in the South China Block leading to profound variations of the local temperature conditions. We processed 201 teleseismic events beneath 87 stations in the Hainan, Guangdong, and Fujian provinces in the South China Block, and extracted 4172 high-quality receiver functions. We imaged the topography of the local mantle discontinuities by using phase-weighted common conversion point stacking of the receiver functions, which effectively improves the P-to-S-converted phases. We found that the average depths of the discontinuities at 410 and 660 km depth are 414 and 657 km, respectively, while no clearly defined discontinuity at 520 km depth was detected. We mapped the thickness of the mantle transition zone (MTZ), which can reflect temperature and/or compositional heterogeneities as well as the presence of water, and discussed possible geodynamic implications. In particular, we found that the MTZ beneath the Leizhou Peninsula in the Hainan province is 42 km thinner than average. This scenario suggests that the Hainan plume is responsible for positive temperature anomalies between ~270 and 380 K and between ~200 and 240 K at the 660 and 410 km discontinuities, respectively. We also observed a prominent uplifting of the 660 km boundary beneath the coast regions that may be indicative of lateral flow of the Hainan plume.

1. Introduction

Located at the intersection of the Eurasian and Philippine plates, the South China Block (SCB) has a complex history of subduction, continental collision, extension-induced magmatism, and intense crust-mantle interaction [*Taylor and Hayes*, 1983; *Briais et al*., 1993; *Huchon et al*., 1998] (Figure 1). Seismic imaging of the deep mantle beneath the SCB is essential for understanding the dynamic mechanisms acting in this region. Previous seismic studies focused on mantle structures imaged through body wave or surface wave tomography [*Huang et al*., 2003; *Lei et al*., 2009; *Li et al*., 2006], wide-angle reflection/refraction surveys [*Xia et al*., 2010; *Zhang et al*., 2011], and teleseismic receiver function simulations [*Ai et al*., 2007; *Gao et al*., 2010]. These models, however, suffer from a poor resolution that renders the imaging of mantle discontinuities difficult owing to sparse seismic array coverage or limitations of the applied methodologies. More comprehensive studies are thus required to image in detail the upper mantle below this region.

In this study, we present three-dimensional, high-resolution P-to-S receiver function images of upper mantle structures beneath the SCB. Results are obtained from a large number of teleseismic events recorded at permanent seismometers located in the Fujian, Guangdong, and Hainan provinces (see Figure 1). The dense and well-crisscrossed raypaths effectively improve the imaging of upper mantle discontinuities. The inferred details of the upper mantle structures provide us with important information to clarify the interaction between shallow processes and the dynamics of the deep mantle.

2. Background

2.1. Geological Setting and Previous Studies

The SCB was widely intruded by granites and vastly covered by Mesozoic igneous rocks [*Zhou and Li*, 2000], indicating that it experienced episodes of intensive volcanism during its geological history. Previous studies

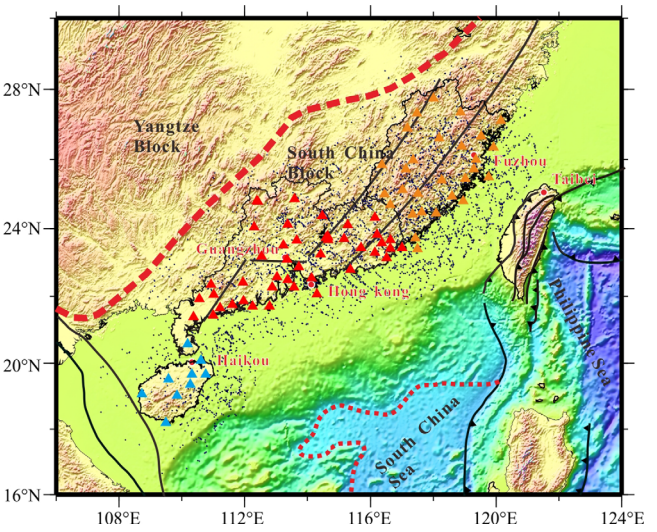

Figure 1. Map showing the study region in the South China Block (SCB) and the seismic stations we used. Orange, red, and cyan triangles denote the permanent stations in Fujian (FJN), Guangdong (GDN), and Hainan (HNN) Seismic Networks, respectively. The thin dotted red line indicates the ocean-continent boundary (OCB), while the bold dashed red line represents the boundary between the Yangtze Block and the SCB. Solid black lines depict some of the main faults in the SCB [after *Ji et al*., 2009]. Jagged lines indicate the locations of trenches to the east of the SCB [after *Rangin and Silver*, 1991]. Black points represent the piercing points of converted *S* waves at a depth of 410 km. Red labeled circles denote provincial capitals around the SCB.

suggest that the paleo-Pacific plate subducted under Southeast Asia in the Mesozoic gave rise to widespread igneous activities [*Jahn et al*., 1976]. *Zhou and Li* [2000] analyzed variations in the age of igneous rocks and inferred that magmatism becomes younger and younger away from the coast.

To the east, Taiwan was formed as one of the youngest orogenic belts owing to the collision between the Philippine and Eurasian plates [*Hsu et al*., 2004] taking place at a rate of ~8.2 cm/yr [*Yu et al*., 1997]. Plate convergence has also influenced the Fujian province, which is separated from Taiwan by the Taiwan Strait.

Global and local seismic travel time tomography have been employed to study the deep structure beneath this region [*Huang and Zhao*, 2006; *Huang et al*., 2010; *Lallemand et al*., 2001], and the results show that prominent low-velocity anomalies (LVA) extending to 400 km are located beneath the SCB and coastal areas. *Huang et al*. [2010] proposed that the subducted plate caused a return flow of lower mantle material into the upper mantle through the mantle transition zone (MTZ). Mesozoic magma chambers associated with the subducted paleo-Pacific plate may have been reheated by hot upwellings leading to the formation of prominent LVAs. In order to investigate the presence of thermal anomalies in the upper mantle, *Ai et al*. [2007] imaged the crust and upper mantle structure beneath southeast China using the receiver function method. According to their results, the thickness of the MTZ seems to be unperturbed, thus indicating a normal thermal environment. However, this study suffers from a relatively poor station coverage being limited to Taiwan and Fujian. Including more stations in southwest districts such as the Guangdong province could help study the relations between the subduction system and the dynamics of the deep mantle in a more comprehensive way.

The Hainan Island, located near the southwestern margin of the SCB, has been affected by the extension of the South China Sea and northward drift of the Indian plate [*Huang et al*., 1998]. A wide range of Cenozoic magma eruptions are distributed in the Hainan Island, and some studies report that the Hainan plume is responsible for a very low-velocity zone beneath this area [*Huang and Zhao*, 2006; *Lebedev and Nolet*, 2003]. However, the depth from which this plume actually originates is yet to be clarified. Using high-quality local and teleseismic data, *Lei et al*. [2009] reported that the plume is characterized by an 80 km wide conduit inclined toward south east that extends from the surface down to a depth of 250 km. They also proposed that the inclination of such upwelling results from mantle flow driven by the subduction of the Philippine plate. However, because of the limited resolution of the data, the authors did not discuss deeper structures extending to the lower mantle, leaving the question as to where the root of the Hainan plume is located still a matter of debate.

2.2. Mineral Physics of Upper Mantle Discontinuities

The MTZ is bounded by two sharp discontinuities at the depths of about 410 and 660 km (hereafter simply called "the 410" and "the 660"). These two discontinuities are traditionally interpreted as phase-transition boundaries marking the exothermic transformation of olivine into wadsleyite and the endothermic transformation of ringwoodite into perovskite (postspinel) [*Ringwood*, 1975; *Bina and Helffrich*, 1994]. Lateral temperature heterogeneities can perturb the equilibrium position of the phase transitions. In a relatively cold environment, in the presence of a slab subducting trough the MTZ, the 410 and 660 km boundaries are, respectively, uplifted and depressed with respect to their equilibrium depths, whereas in a hotter

Figure 2. Epicenter distribution of teleseismic events used in this study. Black stars denote the locations of earthquakes. The dashed circle marks the lowest (30°) epicentral distance of the teleseismic earthquakes from the center of the networks (115.27°E, 24.10°N).

environment associated with a mantle plume, they will be depressed and uplifted instead. Estimating the thickness of the MTZ can thus provide important information about subducted slabs and mantle plumes.

However, it must be noted that standard depth-temperature relations can be complicated by other factors affecting the topography of these discontinuities, such as chemical composition and water content. As *Van der Lee and Wiens* [2006] summarized, increasing water content has opposite effects on the depth and sharpness of the 410 and 660 as compared with those induced by temperature heterogeneities. *Schmerr and Garnero* [2007] suggested that hydrated wadsleyite may remain at the top of the MTZ because of its chemically buoyant nature, giving rise to a localized melt layer atop the 410. The shape of the 660 may also be complicated by the presence of an additional phase change from ringwoodite to ilmenite and deeper to perovskite. Nevertheless, compositional heterogeneities and water content are likely to exert a second-order effect when compared to thermal contrasts [*Eagar et al*., 2010].

3. Data and Methods

3.1. Distribution of Stations and Earthquakes

We used teleseismic seismograms recorded at 87 stations from seismic networks in the Fujian (FJN), Guangdong (GDN), and Hainan (HNN) provinces in the SCB (Figure 1). All of these stations have operated for at least 10 years and accumulated a large amount of seismic data.

We downloaded teleseismic waveforms from the China Earthquake Data Center (CEDC; http://data.earthquake.cn/data/) acquired between January 2000 and December 2008. Earthquake magnitudes are greater than 5.8, and epicentral distances range from 30° to 90° (Figure 2).

3.2. Receiver Function Isolation

The receiver function method is one of the most powerful tools to study the structure of the lithosphere [*Ammon*, 1991; *Langston*, 1979]. In recent years, the process of stacking in exploration seismology has been

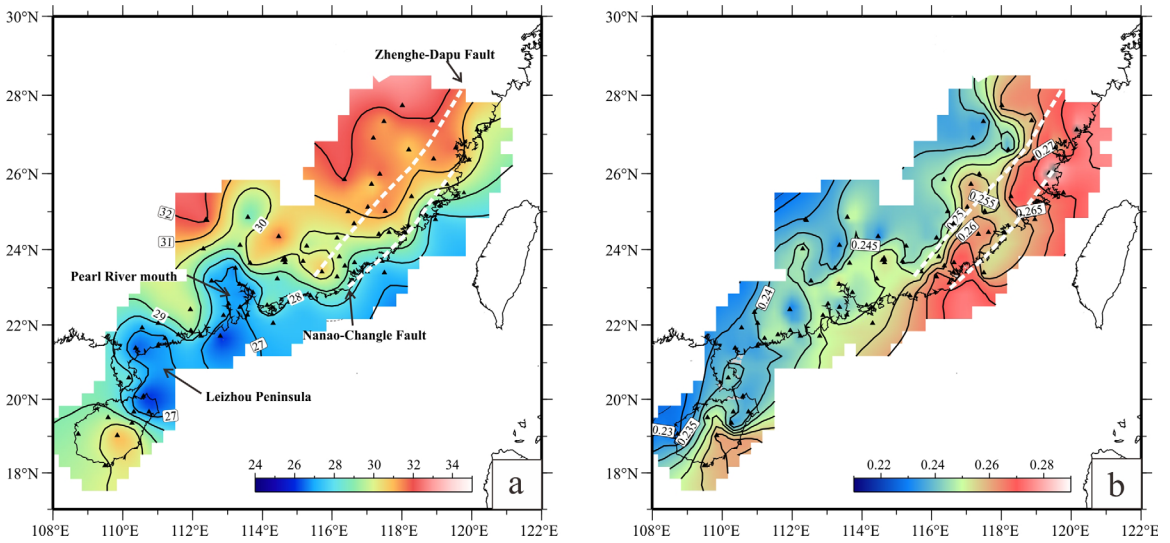

Figure 3. (a) Crustal thicknesses and (b) V_p/V_s ratio in the SCB [after *Huang et al.*, 2012, 2014]. The contours of the crustal thickness and of V_p/V_s are tracked based on the data of 87 stations in the SCB. The dashed white lines denote the Zhenghe-Dapu Fault and Nanao-Changle Fault.

combined with this method to study mantle discontinuities and the MTZ [*Shen et al.*, 1998; *Yuan et al.*, 2000]. In this study, we investigate the topography of the 410 and 660 using high-quality P-to-S receiver functions in order to provide a detailed picture of the structure of the MTZ beneath the SCB.

We manually checked the downloaded seismograms and discarded recordings with invalid data caused by equipment failure. The selected seismograms were windowed to include about 25 s before and 100 s after the theoretical P arrival time calculated from the iasp91 model [*Kennett and Engdahl*, 1991]. A source equalization procedure [*Ammon*, 1991; *Langston*, 1979] was then applied to isolate the receiver functions by deconvolving the vertical components from the radial and tangential components of the seismograms. Receiver functions characterized by a large noise of the prearrival signals or without obvious converted phases have been discarded. We finally obtained 4172 high-quality receiver functions (the data can be downloaded as supporting information from the online version of the paper), with a number of records-per-station varying from 6 to 120. In total, we extracted these waveforms from 201 teleseismic events (Figure 2).

3.3. Phase-Weighted Common Conversion Points Stacking

We constructed an improved 3-D image of the MTZ structure by taking advantage of the phase-weighted common conversion point stacking approach [*Frassetto et al.*, 2010]. First, we prepared a 1-D shear wave velocity model with a depth ranging from 0 to 800 km. We determined crustal thickness (H) and V_p/V_s ratio (κ) via H-κ stacking process (Figure 3) [*Huang et al.*, 2012, 2014]. With this method, amplitudes at the predicted arrival times of the hypothetical P-to-S-converted phases plus their multiples are summed up. The best estimates of H and κ are then obtained by finding the maximum stacking values [*Zhu and Kanamori*, 2000]. We extracted shear wave velocities below the Moho from the global 3-D tomography model SL2013sv of *Schaeffer and Lebedev* [2013] and computed P wave velocity anomalies assuming $\delta\ln\beta/\delta\ln\alpha = 1.4$, where α and β are P and S velocities, respectively.

Second, we calculated the raypath of each receiver function in the depth domain according to ray parameter, coordinates of the station and event, and velocity values corresponding to those of the 1-D model (at 50 s reference period) used by *Schaeffer and Lebedev* [2013] as a reference for their tomographic model. For this calculation, we used a model consisting of 800 parallel spherical layers with a spacing of 1 km. We modified the crustal structure in the 1-D reference model of *Schaeffer and Lebedev* [2013] according to the estimated H and κ to correct shallow heterogeneities around the stations (Figure 4). We then calculated the raypaths of the receiver functions within the first layer on the base of Snell's law. Heterogeneities in the upper mantle have been corrected based on the absolute velocities extracted from the 3-D regional model along the unperturbed raypath. The amplitude of the calculated arrival time in the receiver function was

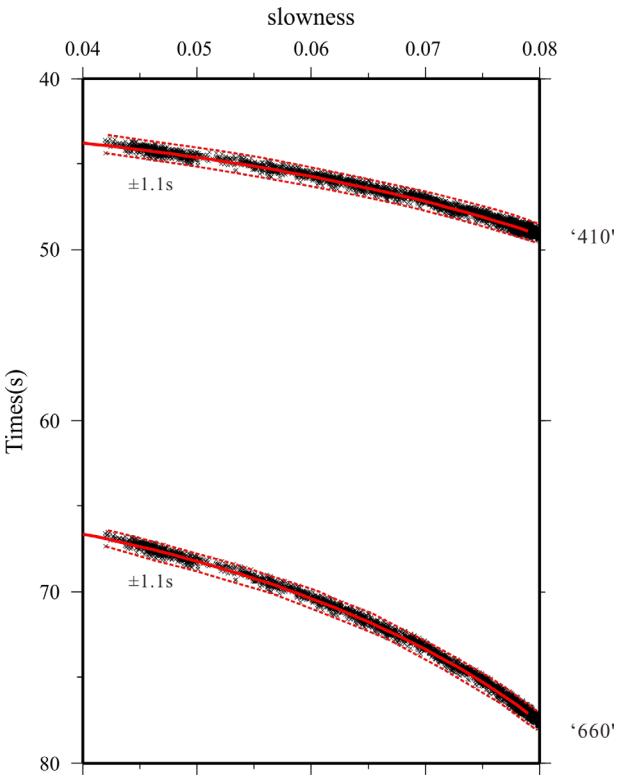

Figure 4. P410s and P660s timing corrections. Solid red lines around 40–45 and 65–70 s denote predicted P410s and P660s moveout curves from the 1-D reference model of *Schaeffer and Lebedev* [2013]. Black crosses mark the travel times predicted by taking the crust heterogeneity around stations into account. Dashed red lines surrounding the moveout curves, which are labeled by the corresponding value, define the ranges of the corrections.

assigned to the location where the P-to-S conversion wave (the piercing point) is generated. In the same way, we calculated the raypath and the relative travel time in the second layer. By repeating this process, we back projected the entire time domain receiver functions onto appropriate conversion depths and associated locations. To suppress high-frequency noise, we also filtered all of the receiver functions using a Butterworth band-pass filter of 0.03–0.3 Hz before the migration.

Finally, our study area was gridded at an interval of 75 km, corresponding to 90% of the Fresnel radius at 410 km depth. Each grid point was considered as a circular bin with a thickness of 1 km extending down to 800 km. Amplitudes at piercing points falling into the same circular bin were phase-weighted stacked using the bootstrapping method [*Efron and Tibshirani*, 1986]. The radius of each bin was set according to the first Fresnel radius at the corresponding stacking depth. According to the phase-weighted stacking method, the Hilbert transform of all receiver functions needs to be computed in order to obtain amplitude and instantaneous phase [*Frassetto et al.*, 2010]. According to *Schimmel and Paulssen* [1997], the transform is carried out as follows:

$$S(z)=r(z)+iH(r(z))=A(z)e^{i\varphi(z)} \tag{1}$$

The depth-converted receiver function $r(z)$ and its Hilbert transform $H(r(z))$ define the real and imaginary components of $S(z)$. The terms $A(z)$ and $\Phi(z)$ represent the amplitudes and the instantaneous phases for a particular depth z, respectively. The stack can be expressed as follows:

$$f(z)=\left[\frac{1}{N}\sum_{j=1}^{N} r_j(z)\right]c(z)^{\upsilon} \tag{2}$$

$$c(z)=\frac{1}{N}\left|\sum_{j=1}^{N} e^{i\varphi(z)}\right| \tag{3}$$

In equation (3), $c(z)$ is the averaged absolute value of the instantaneous phase, N is the number of receiver functions, and the exponent υ in equation (2) varies from 0 to 1 to adjust the sharpness of the filter. In this work, we set υ to 1. For each trace j, the corresponding amplitudes r_j are averaged using the bootstrapping method and then multiplied by the phase-weighting term $c(z)$. This multiplication can reduce amplitudes associated with incoherent arrivals and enhance coherent energy [*Frassetto et al.*, 2010]. We keep the circular bins containing at least 20 receiver functions for stacking ($N \geq 20$; Figure 5).

4. Results

4.1. Depths of the 410 and 660

The time versus ray-parameter (T-p) image, which indicates the stacked amplitudes of the entire data set in 0.001 s/km ray-parameter bins, shows clear seismic discontinuities in the upper mantle (Figure 6a). The clearest arrivals at around 4, 13, and 16 s are expected as converted shear waves along with the

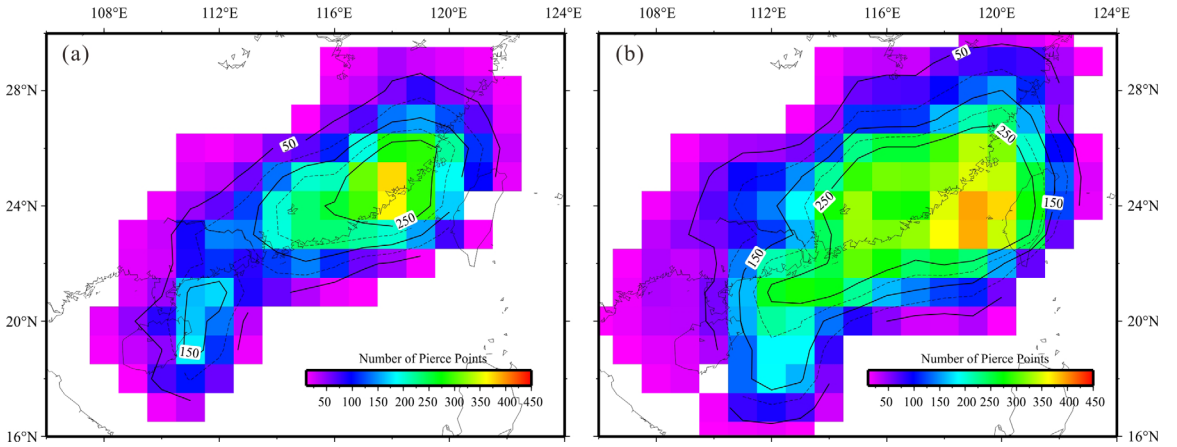

Figure 5. Ray piercing point hit counts for each circular bin. (a) Hit counts of piercing rays at the depth of the 410 km discontinuity, determined by searching the maximum amplitude of the depth-domain receiver function from 370 to 450 km (see section 4.3 for details). (b) Hit counts of piercing rays at the depth of the 660 km discontinuity, determined by searching the maximum amplitude of the depth-domain receiver function from 620 to 700 km. Interval of the histograms is 75 km. The number of rays per bin saturates at 450.

corresponding multiple phases from the Moho. Two other bright arrivals at 45–50 and 65–75 s are identified as converted phases from the 410 (P410s) and 660 (P660s). There is no obvious coherent phase at the predicted time of P520s (near 520 km) as previously reported by *Schmandt et al.* [2012], indicating that the 520 km discontinuity is not a global feature. The stack of all depth-domain receiver functions, determined from SL2013sv, shows peak amplitudes at the average depth of 414 and 657 km, respectively, for P410s and P660s (Figure 6b).

Due to incomplete information on seismic velocities in the upper mantle, the migrated depths of the 410 and 660 are usually not accurate. In order to check this uncertainty, shear wave velocities of the 1-D reference model of *Schaeffer and Lebedev* [2013] were perturbed in a range between −5% and 5% with a 0.5% interval (Figure 7b); for each perturbed model, we calculated the stacked amplitudes and the corresponding depths for P410s and P660s (Figure 7a). The AK135 model [*Kennett et al.*, 1995] was also included in this test. Our results show that the migrated depths vary significantly depending on the seismic velocities. The

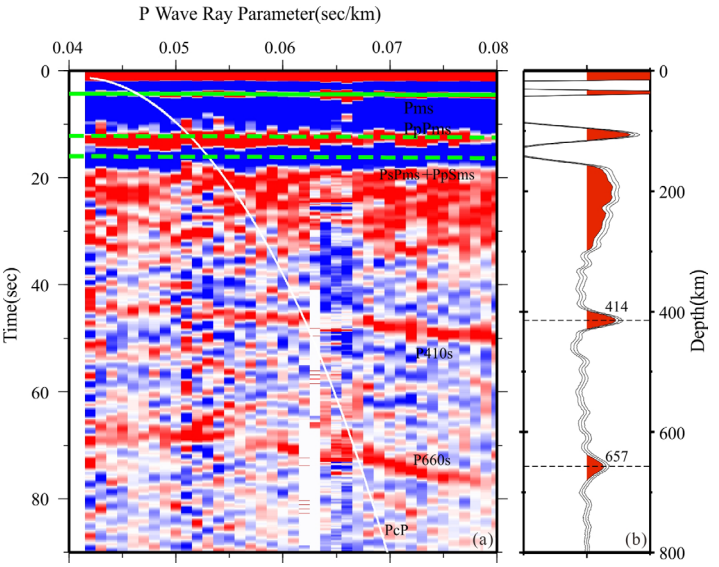

Figure 6. Time versus ray-parameter (T-p) image and depth-migrated cumulative stack. (a) Stacking receiver functions from all stations used in our study. Amplitudes of receiver functions are binned and stacked in 0.001 s/km slowness, and positive amplitudes are shown in red, while negative in blue. P-to-S conversion wave from the Moho (Pms) and multiple phases are marked by solid and broken green lines. The white parabolic line starting from zero time represents the predicted PcP arrival from the iasp91 model. (b) Depth-migrated stacks are shown as black solid lines surrounded by two lines that represent the 95% bootstrap confidence bounds; only the positive amplitudes of receiver functions obtained from SL2013sv model are shown in red. Peak amplitudes of $P_{410}s$ and $P_{660}s$ are labeled by the relevant depths.

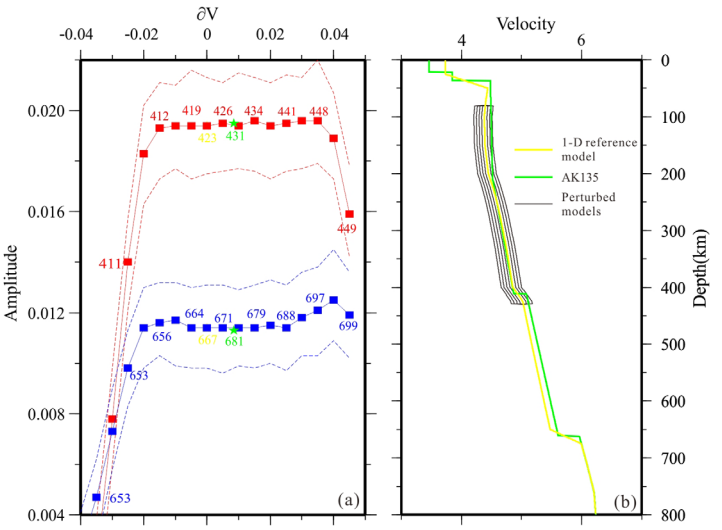

Figure 7. Tests for migrated depths of P410s and P660s using different 1-D models. (a) Stacked amplitudes (*y* coordinate) of the receiver functions at P410s and P660s determined from perturbed 1-D reference models (*x* coordinate) AK135 (green stars). Solid blue lines and solid red lines represent the staked amplitudes for P410s and P660s, respectively, and the corresponding dashed lines represent the 95% bootstrap confidence bounds. The depths for P410s and P660s are labeled at the corresponding data points denoted by squares. (b) Perturbed models in a range between −5% and 5% with a 0.5% interval (thin black lines), 1-D reference model (yellow line), and AK135 (green line).

depths obtained using the 1-D reference model and the AK135 model are, respectively, 423 and 431 km for the 410 boundary and 667 and 681 km for the 660 boundary, while considering the *Schaeffer and Lebedev*'s model perturbed by −1.5%, the depths are 412 and 656 km, which are much closer to the average values determined from SL2013sv [*Lawrence and Shearer*, 2006] (Figure 7a). As revealed by global and regional seismic tomography [*Zhao*, 2004; *Huang et al*., 2010; *Schaeffer and Lebedev*, 2013], velocities below the SCB are relatively low with respect to average conditions. We thus suggest that the real shear wave velocities beneath the SCB are about 1.5% lower than those obtained from the 1-D reference model, as also reported by the 3-D tomography model SL2013sv. By correcting the heterogeneities in the upper mantle with a 3-D tomography model, we can significantly reduce the bias in the depth estimate due to wrong migration models. Furthermore, in this work, we focused mainly on the lateral variations of the upper mantle discontinuities, which are supposed to reflect temperature heterogeneities closely related to the dynamics of the deep mantle.

4.2. Cross Sections Across the Study Region

Figure 8 shows the stacking results in the form of slices extracted from the 3-D stacked receiver function volume, with their location indicated in the geographic map of the SCB in top left figure. For comparison, AA′ and BB′ correspond to the cross sections presented by *Ai et al*. [2007]. CC′ and DD′ lie in GDN, and DD′ passes through the Pearl River mouth where the Moho is clearly uplifted as mentioned in *Huang et al*. [2014] and shown in Figure 3a. EE′ and FF′ lie in HNN with FF′ passing across the Leizhou Peninsula below which the Hainan plume is supposed to be located. All of these six slices have a NW orientation nearly parallel to the extension and subduction directions of the regional tectonic setting, whereas GG′ was chosen to pass through HNN, GDN, and FJN with a NEE orientation in order to image the upper mantle structure, from SW to NE, of the entire SCB.

In FJN (slices AA′ and BB′), the stacked amplitudes are basically consistent with the results presented by *Ai et al*. [2007] at the depths of the 410 and 660, but are also more detailed. This can be due to the accurate correction of the crustal structure beneath the stations obtained through the *H*-κ stacking process, and to corrections of large mantle heterogeneities atop the MTZ obtained using a reliable 3-D shear wave velocity model. In AA′, the 410 is depressed to ∼417 km at 119°E–121°E, while the 660 uplifted to 650 km around 118°E. Right on top of the primary discontinuity at 118°E–110°E, there is a secondary discontinuity at ∼610 km. In BB′, the 660 is mainly unperturbed but shows an uplift from ∼660 to ∼653 km around 110°E, and the stacked amplitudes are sharp and continuous.

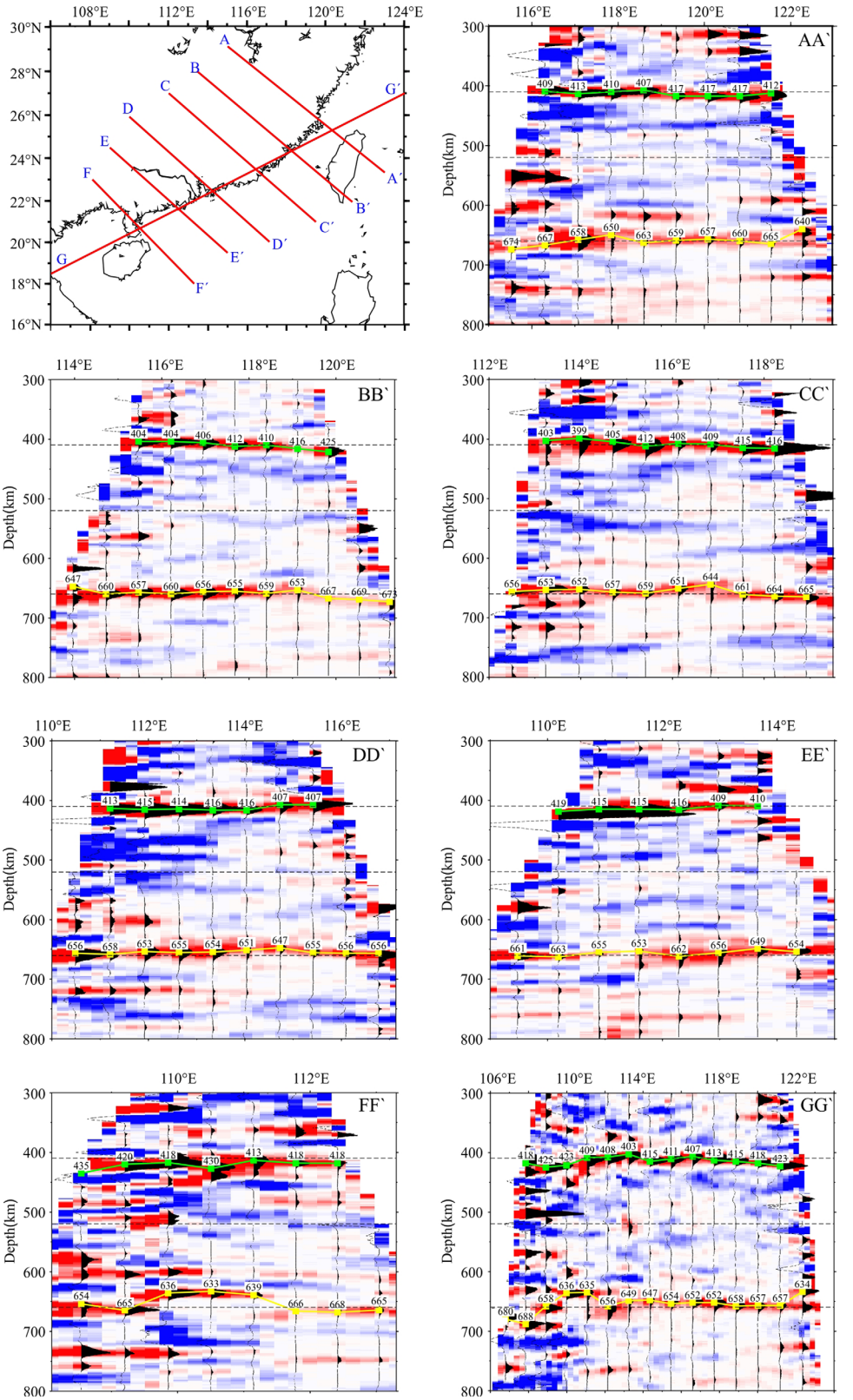

Figure 8. Cross sections throughout the SCB from receiver function amplitudes stacked over 30 km wide bands. The top left figure shows the locations of these cross sections. Positive and negative amplitudes are shown in red and blue, respectively. The predicted depths of the 410 and 660 are indicated by green and yellow lines, respectively. The depth-migrated receiver functions are also shown on the cross sections.

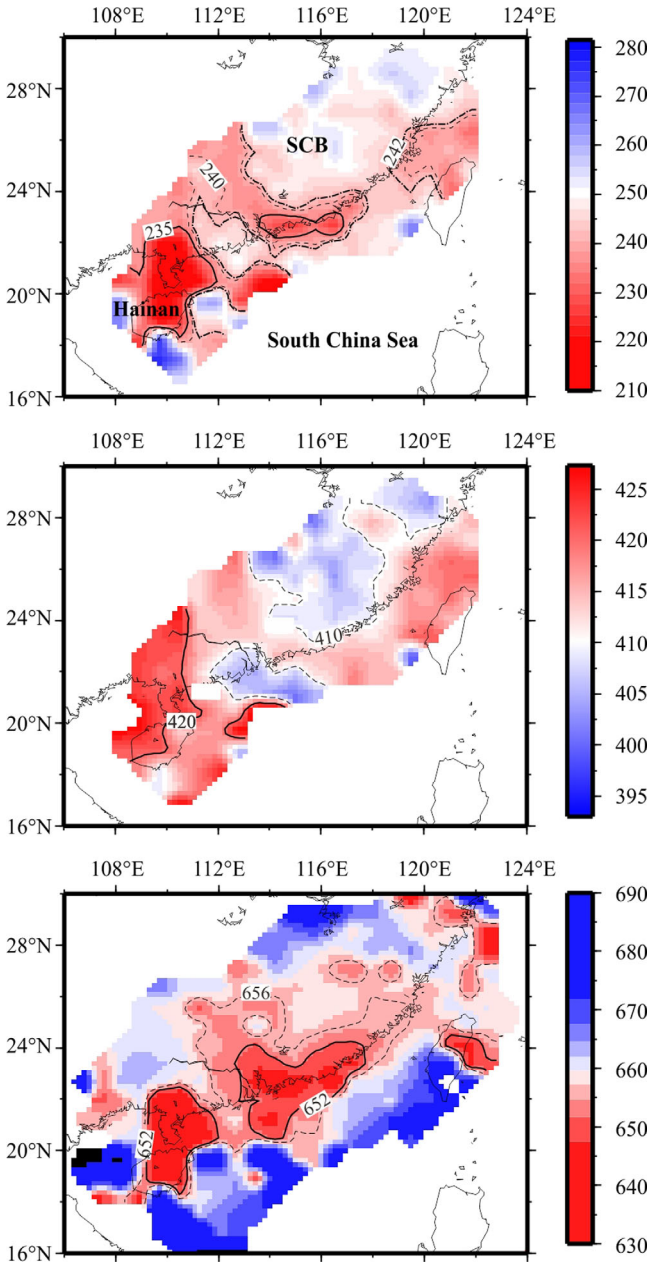

Figure 9. Maps of (a) the transition zone thickness and of the topography of the (b) 410 and (c) 660. The transition zone thickness is calculated by subtracting the depth of the 660 from that of the 410 for each bin. Contour lines denote the thickness and depth variations.

In CC′ and DD′, the depths of the 410 and 660 appear to be stable except that the 660 is clearly raised by 10–15 km at 115°E–117°E in CC′ and DD′, similarly as for the BB′ cross section.

In EE′ and FF′, due to limited data coverage or more noise interference in the receiver functions, the 410 and 660 exhibit a more complex topography with a few uplifts and depressions. For FF′, which passes through the Leizhou Peninsula, a greatly depressed 410 and uplifted 660 are observed at 109°E–111.5°E, indicating the strong influence of the mantle plume.

With its NE orientation, the slice GG′ reveals more clearly the irregular spatial distribution of the 410 and 660 in the SCB. This slice shows very clearly the depression of the 410 and the uplift of the 660 beneath the Leizhou Peninsula. To the northeast, the 660 also shows a clear uplift of up to ~13 km from 114°E to 118°E that diminishes away from the Leizhou Peninsula, while the 410 remains largely unperturbed.

4.3. Topography of the 410 and 660

We determined the depth of the 410 and 660 by automatically picking and recording the maxima of the depth-domain stacked amplitudes in the ranges of 370–450 and 620–700 km.

Figure 9a shows the thickness of the MTZ computed by subtracting the depth of the 660 (Figure 9c) from that of the 410 (Figure 9b). Topographies of the 410 and of the 660 exhibit strong variations throughout the SCB. In the Hainan province, the depth of the 410 reaches more than 420 km and attains its highest value (~430 km) in the north of the Leizhou Peninsula. Within this region, the stacked amplitudes have complex shapes owing to the sparse distribution of the piercing points (Figure 5a). In the Guangdong and Fujian provinces, the 410 has an average depth of 410 km in most of the area and tends to become deeper away from the coast as suggested by the velocity heterogeneities atop the MTZ and shown in the corresponding slices. Compared to the Hainan province, peaks of the stacked amplitudes are sharper and more easily recognizable within this large area.

The 660 is characterized by two major topographic variations in the Leizhou Peninsula and along the coastline. In the former, it appears to be elevated to 636 km within a narrow region surrounded by a prominent depression (~690 km), whereas in the Guangdong and Fujian provinces, it shows an uplift belt of ~15 km along the coastal region from the Pearl River mouth to the northeast of FJN.

The two above features are also evident in the MTZ thickness (Figure 9a), which is less influenced by the heterogeneous upper mantle when compared with the 410 and 660. The MTZ has a minimum thickness of ~208 km in the north of the Leizhou Peninsula, where the 410 and 660 are, respectively, depressed by 18 km and uplifted by 24 km (Figures 9b and 9c). In most parts of the Guangdong and Fujian provinces, the thickness of the MTZ ranges from 235 to 255 km, thus fluctuating around the global average of 250 km predicted by iasp91. An obvious anomalous belt of thinned MTZ extends from the Pearl River mouth to the northeast of Taiwan parallel to the coastline. Regarding this feature, the 410 remains essentially unperturbed while the 660 is uplifted by about 10–15 km.

In order to assess the reliability of the main observed characteristics of the 410, of the 660 and of the MTZ thickness, we compared the migrated results using different global and local 3-D tomography models, namely Grand2000 [*Masters et al*., 1996], MIT09 [*Li et al*., 2008], and HZC [*Huang et al*., 2010]; in addition, we tested other 1-D reference models for comparison. The results show that the most prominent features of the discontinuities variations are basically consistent, which confirms the reliability of our results (see supporting information).

5. Discussion

5.1. Hot Mantle Beneath the Leizhou Peninsula

The topography of MTZ discontinuities is controlled by several factors such as temperature, composition, and water content, with the temperature being generally accepted as the primary one.

We observed a MTZ about 42 km thinner than normal beneath the Leizhou Peninsula in the Hainan province, where the 410 is depressed by ~18 km and the 660 elevated by ~24 km. Assuming a pressure gradient of 33 MPa/km and Clapeyron slopes between 2.5 and 3.0 MPa K^{-1} for the 410 and between −2.0 and −3.0 MPa K^{-1} for the 660 [*Helffrich*, 2000], a positive thermal anomaly between 230 and 308 K can be inferred if this is evenly distributed between the 410 and 660 and the anomalous thickness of the MTZ is solely of thermal origin.

The depressed 410 and uplifted 660 also indicate positive thermal variations of about 200–240 and 270–380 K, respectively, near the two discontinuities (Figure 10). According to *Lebedev et al*. [2003] and the test presented in section 4.1, accurate depth estimates of the 410 and 660 depend on seismic velocities above and within the MTZ. We thus compared the pattern of the topographies of the 410 and 660 boundaries with the seismic tomography model to find their correlation. The topography of the 410 boundary correlates well with velocity anomalies predicted by SL2013sv beneath this area. Assuming that velocity perturbations are of thermal origin and that $\delta \ln \alpha / \delta T = -5 \times 10^{-5}$ from *Karato* [1993], the estimated temperature increase of 200–240 K of the 410 corresponds to velocity perturbations between −1.2 and −1.0% for *P* waves and between −1.4 and −1.6% for *S* waves, which are comparable with those of the tomographic model SL2013sv (Figure 10). However, the topography of the 660 does not correlate as well with the tomographic anomalies. The expected P and S perturbations are, respectively, between −1.3 and −1.5% and between −1.8 and −2.1%, significantly higher than the predictions of the tomography model (−1.0%). This inconsistency may indicate a more complex thermal and compositional state near the 660, which renders velocity variations irregular.

Cenozoic alkali basalts, spread over the SCB, are thought to originate from a deep mantle source [*Li et al*., 1999]. The sources in the Leizhou Peninsula are intermediate between MORB and OIB, indicating that basalts in this area may have been affected by a deep mantle plume [*Zou and Fan*, 2010]. The inferred hot mantle beneath the Leizhou Peninsula supports the presence of the Hainan plume in the mantle transition zone (Figure 10). *Yan and Shi* [2007] calculated the average mantle temperature using the olivine in basalt phenocryst and concluded that the mantle potential temperature in South China Sea adjacent to the SCB is by 200 K higher than average. This estimate compares well with our results and confirms the anomalously hot mantle. Furthermore, the narrow radius (~300 km) of the thinned MTZ implies that the plume should originate from the lower mantle [*Courtillot et al*., 2003; *Zhao et al*., 2011].

5.2. The Deepened 660 Around the Hainan Plume

Surrounding the Leizhou Peninsula we identified a prominent depression of the 660 (up to 690 km) as shown in Figure 8 (GG′) and Figure 10. Using the same Clapeyron slope for the 660, the change in depth

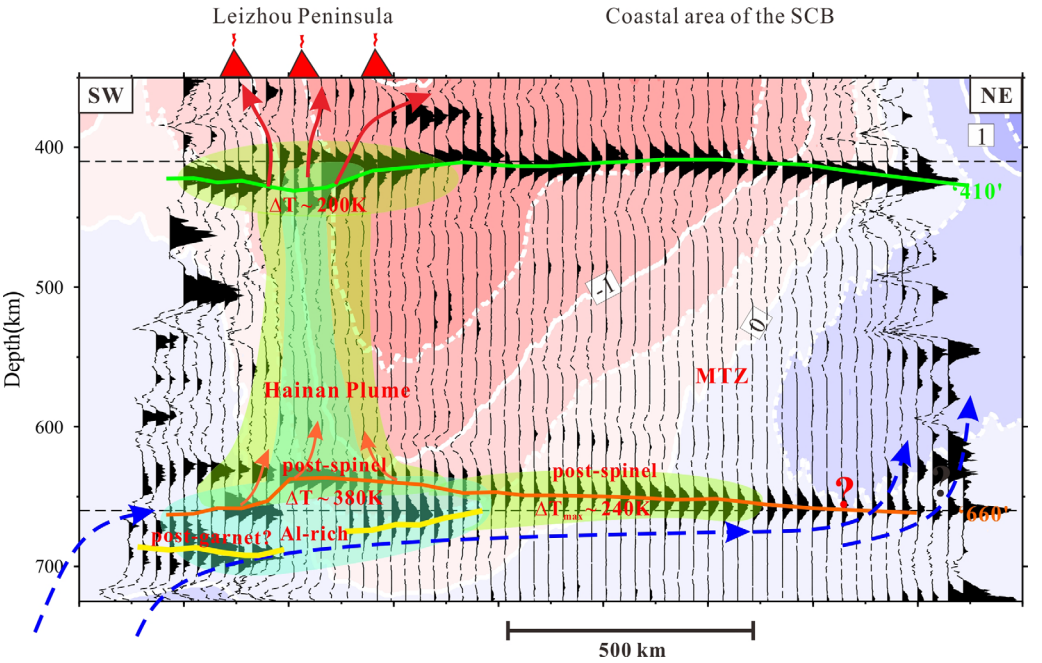

Figure 10. Sketch of the temperature anomaly around the MTZ below the SCB, superimposed on the shear wave velocity tomography (colored and contoured) and the stacked receiver function slice GG′ (Figure 8). Green, brown, and yellow lines indicate interfaces near depths of 410, 660, and 690 km. The deep 410 and shallow 660 below the Leizhou Peninsula suggest temperatures higher than average ($\Delta T_{410} \sim 200$ K and $\Delta T_{660} \sim 380$ K). The interfaces near 690 km (yellow lines) may be indicative of the postgarnet transition owing to Al-rich lower mantle material. Uplifting of the 660 beneath the coastal area of the SCB is consistent with the postspinel transition taking place in an anomalously hot mantle ($\Delta T_{660} \sim 240$ K), possibly induced by lateral flow of the Hainan plume [*Tosi and Yuen*, 2011]. With the current data coverage, we cannot infer the presence of an additional upwelling beneath the eastern part of the study region. The dashed lines indicate possible directions of the mantle flow. Shallow flow paths atop the 410 beneath the Leizhou Peninsula are not resolved by the receiver function method.

from 636 to 690 km would imply a temperature contrast of ~900 K. Such a large temperature variation is unrealistic and implies the presence of lateral variations in composition at the base of MTZ or of changes in the water content. Mineral physical studies [*Weidner and Wang*, 1998; *Hirose*, 2002] show that, at high temperatures and in the presence of alumina (Al), the transition from majorite garnet to perovskite (postgarnet, Figure 10) becomes dominant over the postspinel transition. Our image of the deepened 660 may reveal a change of phase transition relative to the increase in the Al-content of the mantle or the influence of water. The Hainan province is located in an area where different plates converge, forming a reservoir of subducted oceanic crust. Continuous deep subduction and segregation of basaltic layers may have triggered the plume to rise and carry upward hydrated crustal material. As a result, an Al-rich or water-rich mantle plume may be ponding at the base of the MTZ, thereby affecting the topography of the 660 (Figure 10).

5.3. Slight Thinning of the MTZ Along the Coastline

Ai et al. [2007] obtained a normal MTZ below the Fujian province and Taiwan Strait using receiver functions. On the contrary, an anomalous belt of slightly thinned MTZ with a prominent continuity along the coastline is a clear feature emerging from our study. This is a robust anomaly that we identified using different corrections of the topography of the 660 for 3-D heterogeneities (see Figure S1 of the supporting information). In particular, it is clear from the topographies of the 410 and 660 that the uplift of the latter contributes almost entirely to the thinning of the MTZ (Figure 9). Considering the same phase-transition parameters as used for computing thermal variations beneath the Leizhou Peninsula, the shallower 660 (by 10–15 km) suggests a regional thermal perturbation of up to 240 K at the bottom of the MTZ (Figure 10). Unlike the mantle plume passing through the MTZ beneath the Leizhou Peninsula, the hot mantle seems to be confined at the base of the transition zone below the Guangdong and Fujian provinces, forming a region of elevated temperature extending along the coastline.

Responsible for the thinned MTZ under the Leizhou Peninsula could be a secondary upwelling associated with the Hainan plume (Figure 10). In the framework of dynamic simulations, *Tosi and Yuen* [2011] proposed a

model in which plumes may flow laterally beneath the 660, inducing the formation of a local thermal boundary layer, from which one or more secondary upwellings can originate [see also *Kumagai et al*., 2007]. This scenario, which can help explain the enigmatic seismic observation of a vast region of hot material ponding beneath the 660 west of Hawaii [*Cao et al*., 2011], has also been recently invoked by *Civiero et al*. [2015] to account for the seismic evidence of multiple upwellings in the transition zone beneath the northern East-African rift. The 660 km boundary under the Leizhou Peninsula is uplifted over a relatively broad region. Such uplift, however, tends to diminish away from the Hainan plume, possibly because of lateral flow of hot mantle material. The significant elevation of the 660 in the NE corner of the region (Figure 9) may be due to a secondary upwelling that has not reached the 410 or has already penetrated the MTZ but is not revealed by our data (Figure 10). According to this picture, we speculate that the plume may be located in the SW corner of the study region, in agreement with previous tomography studies, which found that a prominent low-velocity zone in the lower mantle exists around the Indochina peninsula and gradually tilts toward NE [*Huang and Zhao*, 2006]. However, reliability of the tomography model is still crucial for supporting this assumption.

6. Conclusions

Using 4172 receiver functions from 87 stations belonging to local seismic networks of Guangdong, Fujian, and Hainan provinces, we probed the upper mantle discontinuities beneath the SCB. We also determined the topography of the 410 and 660 and the thickness of the mantle transition zone.

The boundaries of the 410 and 660 km discontinuities can be clearly identified throughout the region. The thickness of the transition zone as measured by phase-weighted stacking of the receiver functions is characterized by a prominent thinning of up to 42 km beneath the Leizhou Peninsula and the Hainan Island, suggesting that the Hainan plume causes a local mean temperature increase in the transition zone between 230 and 308 K, depending on the Clapeyron slope of the phase boundaries, with corresponding thermal anomalies at 660 and 410 km depth between 270 and 380 K and between 200 and 240 K, respectively. The inferred thin belt in the MTZ beneath the Guangdong and Fujian provinces is interpreted in terms of elevated temperatures along the coastal areas possibly induced by a channel flow of the mantle plume from SW to NE.

Acknowledgments

We thank the Editor Thorsten Becker and two anonymous reviewers for their thoughtful and constructive comments that significantly helped to improve previous versions of the manuscript. Supporting data are included as Figure S1 and Data Set S1; any additional data presented in this study can be obtained from Haibo Huang (e-mail: go223@scsio.ac.cn). We thank Xuzhang Shen for discussing about the codes of the time-depth migration of the receiver functions and Andy Frassetto for important discussions about the phase-weighted CCP stacking methods. We are grateful to A. J. Schaeffer for providing the tomography model SL2013sv. All of the waveforms were provided by CEDC. All of the figures presented in this article were plotted with the GMT software package [*Wessel and Smith*, 1995]. This study has been supported by the National Nature Science Foundation of China (grant 41306046 and 41222039), the Frontier Program in Young Talents Field of the South China Sea Institute of Oceanology, Chinese Academy of Sciences (SQ201210). N. Tosi acknowledges support from the Helmholtz Association (project VH-NG-1017).

References

Ai, Y. S., Q. F. Chen, F. Zeng, X. Hong, and W. Y. Ye (2007), The crust and upper mantle structure beneath southeastern China, *Earth Planet. Sci. Lett.*, *260*, 549–563.

Ammon, C. J. (1991), The isolation of receiver effects from teleseismic P-wave-forms, *Bull. Seismol. Soc. Am.*, *81*, 2504–2510.

Bina, C. R., and G. Helffrich (1994), Phase transition Clapeyron slopes and transition zone seismic discontinuity topography, *J. Geophys. Res.*, *99*, 15,853–15,860.

Briais, A., P. Patriat, and P. Tapponnier (1993), Updated interpretation of magnetic anomalies and sea floor spreading stages in the South China Sea: Implications for the Tertiary tectonics of Southeast Asia, *J. Geophys. Res.*, *98*, 6299–6328.

Cao, Q., R. D. Van der Hilst, M. V. De Hoop, and S. H. Shim (2011), Seismic imaging of transition zone discontinuities suggests hot mantle west of Hawaii, *Science*, *332*(6033), 1068–1071.

Civiero, C., et al. (2015), Multiple mantle upwellings in the transition zone beneath the northern East African Rift System from relative P wave travel time tomography, *Geochem. Geophys. Geosyst.*, *16*, doi:10.1002/2015GC005948, in press.

Courtillot, V., A. Davaille, J. Besse, and J. Stock (2003), Three distinct types of hotspots in the Earth's mantle, *Earth Planet. Sci. Lett.*, *205*, 295–308.

Eagar, K. C., M. J. Fouch, and D. E. James (2010), Receiver function imaging of upper mantle complexity beneath the Pacific Northwest, United States, *Earth Planet. Sci. Lett.*, *297*, 141–153.

Efron, B., and R. Tibshirani (1986), Bootstrap methods for standard errors, confidence intervals, and other measures of statistical accuracy, *Stat. Sci.*, *1*, 54–75.

Frassetto, A., G. Zandt, H. Gilbert, T. J. Owens, and C. H. Jones (2010), Improved imaging with phase-weighted common conversion point stacks of receiver functions, *Geophys. J. Int.*, *182*, 368–374.

Gao, Y. A., D. Suetsugu, Y. Fukao, M. Obayashi, Y. T. Shi, and R. F. Liu (2010), Seismic discontinuities in the mantle transition zone and at the top of the lower mantle beneath eastern China and Korea: Influence of the stagnant Pacific slab, *Phys. Earth Planet. Inter.*, *183*, 288–295.

Helffrich, G. (2000), Topography of the transition zone seismic discontinuities, *Rev. Geophys.*, *38*, 141–158.

Hirose, K. (2002), Phase transitions in pyrolitic mantle around 670-km depth: Implications for upwelling of plumes from the lower mantle, *J. Geophys. Res.*, *107*(B4), 2078, doi:10.1029/2001JB000597.

Hsu, S. K., Y. Yeh, W. B. Doo, and C. H. Tsai (2004), New bathymetry and magnetic lineations identifications in the northernmost South China Sea and their teconic implications, *Mar. Geophys. Res.*, *25*, 29–44.

Huang, H. B., X. L. Qiu, and S. H. Xia (2012), Crustal structure and Poisson's ratio beneath the Hainan Island, *J. Trop. Oceanogr.*, *31*, 65–70.

Huang, H. B., X. W. Guo, S. H. Xia, and X. L. Qiu (2014), Study of crustal thickness and Poisson's ratio in the coastal area of South China, *Chin. J. Geophys.*, *57*(12), 3896–3906.

Huang, J. L., and D. P. Zhao (2006), High-resolution mantle tomography of China and surrounding regions, *J. Geophys. Res.*, *111*, B09305, doi:10.1029/2005JB004066.

Huang, X., Z. Chen, S. Zhong, S. He, K. Luo, H. Chen, and Y. Qin (1998), *The Instructions of the Digital Geological Map of the Hainan Province*, Hainan Bur. of Geol. and Miner. Explor. and Dev., Haikou, China.

Huang, Z. C., L. S. Wang, D. P. Zhao, M. J. Xu, N. Mi, D. Y. Yu, H. Li, and C. Li (2010), Upper mantle structure and dynamics beneath Southeast China, *Phys. Earth Planet. Inter. 182*, 161–169.
Huang, Z. X., W. Su, Y. J. Peng, Y. J. Zheng, and H. Y. Li (2003), Rayleigh wave tomography of China and adjacent regions, *J. Geophys. Res.*, *108*(B2), 2073, doi:10.1029/2001JB001696.
Huchon, P., T. Nguyen, and N. Chamot-Rooke (1998), Finite extension across the South Vietnam basins from 3D gravimetric modelling: Relation to South China Sea kinematics, *Mar. Pet. Geol.*, *15*, 619–634.
Jahn, B. M., P. Y. Chen, and T. P. Yen (1976), Rb-Sr ages of granitic rocks in Southeastern China and their tectonic significance, *Geol. Soc. Am. Bull.*, *87*, 763–776.
Ji, S. C., Q. Wang, and M. H. Salisbury (2009), Composition and tectonic evolution of the Chinese continental crust constrained by Poisson's ratio, *Tectonophysics*, *463*, 15–30.
Karato, S. I. (1993), Importance of anelasticity in the interpretation of seismic tomography, *Geophys. Res. Lett.*, *20*, 1623–1626.
Kennett, B., and E. Engdahl (1991), Traveltimes for global earthquake location and phase identification, *Geophys. J. Int.*, *105*, 429–465.
Kennett, B., E. Engdahl, and R. Buland (1995), Constraints on seismic velocities in the Earth from travel-times, *Geophys. J. Int.*, *122*, 108–124.
Kumagai, I., A. Davaille, and K. Kurita (2007), On the fate of thermally buoyant mantle plumes at density interfaces, *Earth Planet. Sci. Lett.*, *254*, 180–193, doi:10.1016/j.epsl.2006.11.029.
Lallemand, S., Y. Font, H. Bijwaard, and H. Kao (2001), New insights on 3-D plates interaction near Taiwan from tomography and tectonic implications, *Tectonophysics*, *335*, 229–253.
Langston, C. A. (1979), Structure under Mount Rainier, Washington, inferred from teleseismic body waves, *J. Geophys. Res.*, *84*, 4749–4762.
Lawrence, J. F., and P. M. Shearer (2006), A global study of transition zone thickness using receiver functions, *J. Geophys. Res.*, *111*, B06307, doi:10.1029/2005JB003973.
Lebedev, S., and G. Nolet (2003), Upper mantle beneath southeast Asia from S velocity tomography, *J. Geophys. Res.*, *108*(B1), 2048, doi: 10.1029/2000JB000073.
Lebedev, S., S. Chevrot, and R. D. van der Hilst (2003), Correlation between the shear-speed structure and thickness of the mantle transition zone, *Phys. Earth Planet. Inter.*, *136*(2003), 25–40.
Lei, J. S., D. P. Zhao, B. Steinberger, B. Wu, F. L. Shen, and Z. X. Li (2009), New seismic constraints on the upper mantle structure of the Hainan plume, *Phys. Earth Planet. Inter.*, *173*, 33–50.
Li, C., R. D. van der Hilst, and A. N. Toksoz (2006), Constraining P-wave velocity variations in the upper mantle beneath Southeast Asia, *Phys. Earth Planet. Inter.*, *154*, 180–195.
Li, C., R. D. van der Hilst, E. R. Engdahl, and S. Burdick (2008), A new global model for P wave speed variations in Earth's mantle, *Geochem. Geophys. Geosyst.*, *9*, Q05018, doi:10.1029/2007GC001806.
Li, Z. X., X. H. Li, P. D. Kinny, and J. Wang (1999), The breakup of Rodinia: Did it start with a mantle plume beneath South China?, *Earth Planet. Sci. Lett.*, *173*, 171–181.
Masters, G., S. Johnson, G. Laske, H. Bolton, and J. H. Davies (1996), A shear-velocity model of the mantle (and discussion), *Philos. Trans. R. Soc. London A*, *354*, 1385–1411.
Rangin, C., and E. A. Silver (1991), Neogene tectonic evolution of the Celebes-Sulu basins: New insights from Leg 124 drilling, *Proc. Ocean Drill. Program Sci. Results*, *124*, 51–63.
Ringwood, A. E. (1975), *Composition and Petrology of the Earth's Mantle*, McGraw-Hill, N. Y.
Schaeffer, A. J., and S. Lebedev (2013), Global shear-speed structure of the upper mantle and transition zone, *Geophys. J. Int.*, *194*, 417–449.
Schimmel, M., and H. Paulssen (1997), Noise reduction and detection of weak, coherent signals through phase-weighted stacks, *Geophys. J. Int.* *130*(2), 497–505.
Schmandt, B., K. Dueker, E. Humphreys, and S. Hansen (2012), Hot mantle upwelling across the 660 beneath Yellowstone, *Earth Planet. Sci. Lett.*, *331*, 224–236.
Schmerr, N., and E. J. Garnero (2007), Upper mantle discontinuity topography from thermal and chemical heterogeneity, *Science*, *318*, 623–626.
Shen, Y., A. F. Sheehan, K. G. Dueker, C. de Groot-Hedlin, and H. Gilbert (1998), Mantle discontinuity structure beneath the southern East Pacific Rise from P-to-S converted phases, *Science*, *280*, 1232–1235.
Taylor, B., and D. E. Hayes (1983), Origin and history of the South China Sea basin, in *The Tectonic and Geologic Evolution of Southeast Asian Sea and Islands*, edited by D. E. Hayes, pp. 23–56, AGU, Washington, D. C.
Tosi, N., and D. A. Yuen (2011), Bent-shaped plumes and horizontal channel flow beneath the 660 km discontinuity, *Earth Planet. Sci. Lett.*, *312*, 348–359.
Van der Lee, S., and D. A. Wiens (2006), Seismological constraints on Earth's deep water cycle, in *Earth's Deep Water Cycle, Geophys. Monogr. Ser.*, vol. 168, pp. 13–27, AGU, Washington, D. C.
Weidner, D. J., and Y. Wang (1998), Chemical- and Clapeyron-induced buoyancy at the 660 km discontinuity, *J. Geophys. Res.*, *103*, 7431–7441.
Wessel, P., and W. H. Smith (1995), New version of the generic mapping tools, *Eos Trans. AGU*, *76*, 329.
Xia, S., M. Zhao, X. Qiu, H. Xu, and X. Shi (2010), Crustal structure in an onshore–offshore transitional zone near Hong Kong, northern South China Sea, *J. Asian Earth Sci.*, *37*, 460–472.
Yan, Q. S., and X. F. Shi (2007), Hainan mantle plume and the formation and evolution of the South China Sea [in Chinese], *Geol. J. China Univ.*, *13*(2), 311–322.
Yu, S. B., H. Y. Chen, and L. C. Kuo (1997), Velocity field of GPS stations in the Taiwan area, *Tectonophysics*, *274*, 41–59.
Yuan, X., et al. (2000), Subduction and collision processes in the Central Andes constrained by converted seismic phases, *Nature*, *408*, 958–961.
Zhang, Z. J., L. Q. Yang, J. W. Teng, and J. Badal (2011), An overview of the earth crust under China, *Earth Sci. Rev.*, *104*, 143–166.
Zhao, D. P. (2004), Global tomographic images of mantle plumes and subducting slabs: Insight into deep Earth dynamics, *Phys. Earth Planet. Inter.*, *146*(1–2), 3–34.
Zhao, D. P., S. Yu, and E. Ohtani (2011), East Asia: Seismotectonics, magmatism and mantle dynamics, *J. Asian Earth Sci.*, *40*, 689–709.
Zhou, X. M., and W. X. Li (2000), Origin of Late Mesozoic igneous rocks in Southeastern China: Implications for lithosphere subduction and underplating of mafic magmas, *Tectonophysics*, *326*, 269–287.
Zhu, L. P., and H. Kanamori (2000), Moho depth variation in southern California from teleseismic receiver functions, *J. Geophys. Res.*, *105*, 2969–2980.
Zou, H., and Q. Fan (2010), U–Th isotopes in Hainan basalts: Implications for sub-asthenospheric origin of EM2 mantle endmember and the dynamics of melting beneath Hainan Island, *Lithos*, *116*, 145–152.